

View Article Online
View Journal

Journal of Materials Chemistry A

Materials for energy and sustainability

Accepted Manuscript

This article can be cited before page numbers have been issued, to do this please use: C. Ma, N. Zhang, D. Wang, J. Ren, T. Jiang, T. Liu, A. A. Zverko, H. Zhong and X. Zhang, *J. Mater. Chem. A*, 2025, DOI: 10.1039/D5TA07271A.



This is an Accepted Manuscript, which has been through the Royal Society of Chemistry peer review process and has been accepted for publication.

Accepted Manuscripts are published online shortly after acceptance, before technical editing, formatting and proof reading. Using this free service, authors can make their results available to the community, in citable form, before we publish the edited article. We will replace this Accepted Manuscript with the edited and formatted Advance Article as soon as it is available.

You can find more information about Accepted Manuscripts in the <u>Information for Authors</u>.

Please note that technical editing may introduce minor changes to the text and/or graphics, which may alter content. The journal's standard <u>Terms & Conditions</u> and the <u>Ethical guidelines</u> still apply. In no event shall the Royal Society of Chemistry be held responsible for any errors or omissions in this Accepted Manuscript or any consequences arising from the use of any information it contains.



SCHOLARONE™ Manuscripts

Open Access Article. Published on 22 10 2025. Downloaded on 2025/11/03 15:12:59.

This article is licensed under a Creative Commons Attribution-NonCommercial 3.0 Unported Licence

View Article Online DOI: 10.1039/D5TA07271A

Balancing Ru-O Bond Covalency and Strength via Atomically Ta Doping for Robust Acidic Oxygen Evolution

Caini Ma^{‡, a, b}, Ning Zhang^{‡, c}, Depeng Wang^{a, b}, Jian Ren^{a, b}, Tao Jiang^{a, b}, Tong Liu^{a, b, d}, Alexandra A. Zverko^c, Haixia Zhong^{*} a, b, d and Xinbo Zhang^{*, a, b, d}

Received 00th January 20xx, Accepted 00th January 20xx

DOI: 10.1039/x0xx00000x

Ruthenium dioxide electrocatalysts hold the promise of high oxygen evolution reaction activity in proton exchange membrane water electrolyser (PEMWE). However, control of its stability remains extremely challenging due to the easy oxidation and dissolution during electrochemical reaction. Herein, we address this challenge by constructing atomically dispersed Ta-O-Ru asymmetric local motifs for efficient and stable OER process via a simple molten salt assisted method. The optimized candidate (RuO_x-10Ta) exhibits a low overpotential of 189 mV and high durability exceeding 700 hours at 10 mA cm⁻², boasting a sixfold longer lifespan than commercial RuO₂. In-situ characterizations and DFT calculations reveal that, in this asymmetric configuration, high-valent Ta dopants downshift the O 2p and Ru 4d band centres, and thus moderate Ru-O covalency to facilitate water dissociation and intermediate transformation. Meanwhile, this Ta-O-Ru motif with robust Ta-O bond acts as an electron and structure buffer that suppresses lattice oxygen loss and Ru overoxidation, enhancing the overall catalyst stability. When integrated into a PEMWE device as anode catalyst, a low cell voltage of 1.639 V at 1 A cm⁻² and sustained stable operation for over 200 hours at 200 mA cm⁻² were achieved. These findings highlight the potential of asymmetric coordination engineering as a generalizable strategy for developing robust and efficient OER catalysts under harsh acidic conditions.

1 Introduction

Proton exchange membrane water electrolysis (PEMWE), featuring rapid response to intermittent renewable electricity (*e. g.* solar, wind), compact design, and high-purity hydrogen production¹⁻⁴, is pivotal in decarbonized energy systems. Nevertheless, its efficiency is fundamentally constrained by the sluggish anodic oxygen evolution reaction (OER)^{5, 6} and the fast deactivation of catalysts^{7, 8}. Although IrO₂ represents the state-of-the-art acidic OER catalyst, the scarcity and prohibitive cost of iridium severely impede the large-scale PEMWE deployment⁹⁻¹¹. In contrast, Ru-based catalysts, offering better economic feasibility and superior activity, are emerging as a promising alternative for acidic OER¹²⁻¹⁴. Despite the promising attributes, bulk RuO₂ catalysts undergo structural degradation that stems from the inherent electronic structure. In essence, strong Ru-O covalency in ruthenium oxides enables the activation of lattice oxygen and participation in OER process, thereby significantly improving

catalytic activity¹⁵. Unfortunately, such involvement of lattice oxygen accelerates the generation and outward diffusion of oxygen vacancies, progressively eroding the structural integrity. Concomitantly, the removal of lattice oxygen raises the local Ru valence and promotes the formation of high-valent and volatile RuO₄, leading to the irreversible loss of active sites¹³⁻¹⁷. Consequently, it is crucial to balance activity and stability in RuO₂ with fine tuning the electronic structure toward efficient and stable OER.

To break the activity-stability trade-off, several strategies, including strain engineering^{16, 17}, defect engineering^{18, 19}, interface engineering²⁰⁻²², high-entropy alloy design²³ and heteroatom incorporation²⁴⁻³⁰ have been explored. Among these, the foreign atom doping offers a powerful approach to directly modify the local catalytic microenvironment for activity enhancement. Concurrently, effective doping can optimize the electronic configuration of active sites and enhance atomic cohesion, thereby suppressing lattice oxygen loss and ruthenium dissolution. For example, Guo et al. demonstrated that Er doping results in the 4d-2p-4f hybridization in Er doped RuO₂ catalyst, which continuously tunes Ru-O covalency, increases Ru/Ovacancy formation energies and strengthens oxygen intermediate adsorption, thus resulting in the enhanced activity and stability²⁹. In this context, developing an asymmetric M-O-Ru active motif with an optimized local structure through metal atom doping engineering is attractive to boost effective and stable OER process. To avoid the nonuniform doping sites or even phase separation that will sacrifice the mass activity31, key criteria are necessary for rational doping engineering toward building the asymmetric Ru active motif including: i) Lattice compatibility with the matched ionic radii between M and the host cation Ru⁴⁺, which ensures the stable solidsolution formation with rich atomic interfaces and no inert phase

[&]quot;State Key Laboratory of Rare Earth Resource Utilization, Changchun Institute of Applied Chemistry, Chinese Academy of Sciences, No. 5625, Renmin Street, Chaoyang District, Changchun City, Jilin, 130022, P. R. China. E-mail: hxzhong@ciac.ac.cn, xbzhang@ciac.ac.cn

^bSchool of Applied Chemistry and Engineering, University of Science and Technology of China, No. 96, Jinzhai Road, Baohe District, Hefei, Anhui, 230026, P. R. China.

^cState Key Laboratory of Critical Metals Beneficiation, Metallurgy and Purification, Zhengzhou University, No. 100, Kexuedadao Road, Zhongyuan District, Zhengzhou City, Henan, 450001, P. R. China.

^dChina-Belarus Belt and Road Joint Laboratory on Advanced Materials and Manufacturing, Changchun Institute of Applied Chemistry

Chinese Academy of Sciences, 5625 Renmin Street, Changchun 130022, China

^eFaculty of Mechanical Engineering, Belarusian National Technical University

^{65,} Nezavisimosti Ave., 220072, Minsk, Republic of Belarus

[‡] These authors contributed equally to this work.

Dpen Access Article. Published on 22 10 2025. Downloaded on 2025/11/03 15:12:59.

No This article is licensed under a Creative Commons Attribution-NonCommercial 3.0 Unported Licence

segregation^{32, 33}; ii) Lattice-oxygen buffering through strong M-O interactions for stabilizing lattice oxygen, suppressing V_O aggregation and the collapse of Ru oxide lattice³⁴; iii) Electron buffering capability for the dynamic charge redistribution in M-O-Ru linkages, which is favourable for fine-tuning of Ru-O covalency and the adjustable valence state of M against oxidation condition³⁵.

Herein, we present the example of atomically dispersed Ta-O-Ru asymmetric centres for robust OER through Ta doping regarding the strong Ta-O bond (839 kJ/mol)^{36, 37}, higher and adaptable valence (+5 vs Ru⁴⁺)³⁴ and similar ionic radius (Ta⁵⁺ 64 pm \approx Ru⁴⁺ 62 pm)³⁸. The resulting atomic dispersion of Ta within RuOx matrix enables finely modulated local environments of Ru and O sites. Both experimental results and theoretical calculations reveal that the asymmetric Ta-O-Ru unit, characterized by moderate Ru-O covalency and strong Ta-O-Ru linkage, effectively promotes the lattice oxygen participated OER process, wherein excessive lattice oxygen loss and Ru overoxidation are simultaneously suppressed. As expected, the optimized RuO_x-10Ta exhibits high OER performance with an outstanding mass activity of 2.43 A mg_{Ru}-1 at 1.5 V vs. RHE, which is 62% higher than the pristine RuO_x and 13-fold superior to commercial RuO₂. This is achieved alongside a low overpotential of 189 mV at 10 mA cm⁻² and remarkable stability exceeding 700 h at 10 mA cm⁻² in 0.5 M H₂SO₄ (6-fold superior to commercial RuO2), ranking among the most advanced Ru-based OER catalysts. Furthermore, a PEMWE device equipped with RuO_x-10Ta anode demonstrated a low cell voltage of 1.639 V at 1 A cm⁻² and maintained stable operation for over 200 hours at 200 mA cm⁻², highlighting its good feasibility for the practical application. Our work highlights the potential of rationally developing atomically dispersed M-O-Ru asymmetric centres for acidic OER.

2 Results and discussion

2.1 Preparation and structure characterization

A series of tantalum-doped Ru oxide nanoparticles (RuO_x- α Ta, α = 5, 10, 20, corresponding to nominal Ta loadings of 5%, 10%, and 20%, respectively) and pristine RuOx were synthesized via a modified molten salt assisted method (see details in the Supporting Information, Fig. S1) 40, 41. The molten NaNO₃ was used to facilitate the metal-ion exchange and oxide formation. X-ray diffraction (XRD) patterns showed that all RuO_x- α Ta (α = 5, 10, 20) and RuO_x presented a similar single rutile phase compared to C-RuO₂ (commercial RuO₂), with no detectable impurities from Ta₂O₅ (Fig. S2). A systematic downshift of the diffraction peaks is observed as Ta content increases, which is likely due to lattice expansion caused by the substitution of Ru with the larger Ta atoms. SEM imaging combined with elemental mapping (Fig. S3) indicated that the RuOx-10Ta sample consists of interconnected nanoparticles, wherein Ru, Ta, and O elements are uniformly distributed without detectable Na signal, suggesting the effective removal of NaNO₃ salt after synthesis. Inductively coupled plasma mass spectrometry (ICP-MS, Table S1) confirmed that the elemental composition of RuOx-10Ta closely matches the nominal loading values. In addition, transmission electron microscopy (TEM) images (Fig. 1a and Figs. S4-S5) show well-dispersed nanoparticles for RuO_x-5Ta/10Ta/20Ta with an average size of ~7.8 nm, slightly smaller than home-made RuO_x (9.3 nm, Fig. S6). The slight reduction in particle size upon Ta incorporation can be attributed to the effect of dopants on nucleation dynamics during molten synthesis⁴² In Fig. 1b. well-resolved lattice fringes with d-spacings of 0.32 har are attiffed to the (110) planes of rutile RuO₂ phase, similar to those of C-RuO₂ (Fig. S7). The selected area electron diffraction (SAED) pattern analysis (inset of Fig. 1b) confirms the polycrystalline rutile structure with clear (110), (101), (211) and (200) diffraction rings for RuO_x-10Ta and no detectable Ta₂O₅ signatures, which is well consistent with XRD results. In addition, the energy-dispersive X-ray spectra (EDS, Fig. S8) and elemental mapping together with EDS line-scans (Fig. S9) demonstrate the homogeneous distribution of Ta throughout RuO_x nanoparticles. As shown in Fig. 1d, the aberration-corrected high-angle annular dark field scanning transmission electron microscopy (HAADF-STEM) image reveals that Ta atoms were atomically dispersed throughout the lattice of RuOx matrix. It was found that Ta (Z = 73) dopants appeared as isolated and significantly brighter dots within the atom columns (encircled in red), owing to their stronger electron scattering compared to the surrounding Ru (Z = 44) and O (Z = 8) atoms. The distinct atomic-scale distribution was further corroborated by 3D Gaussian fitting mapping (Fig. 1e) and intensity profile analysis (Fig. 1f). These results evidence the high dispersity of the Ta dopants, which implies abundant Ta-O-Ru motifs. Raman spectroscopy was used to further investigate the crystal structure of RuO_x-10Ta (Fig. S10). The absence of discernible peaks assignable to crystalline Ta₂O₅ exclude the phase segregation. Three peaks which can be assigned to Eg, A₁g and B₂g modes of rutile RuO₂ are broadened compared to the pristine RuO_x²⁸, which is associated with the fact that the substitutional doping of Ta impaired the crystalline symmetry^{43, 44}.

X-ray photoelectron spectroscopy (XPS) was performed to characterize the chemical states and the electronic configurations of the catalysts (Fig. S11). In the Ta 4f region (Fig. S11b), two peaks centred at 24.95 eV and 26.85 eV are assignable to Ta 4f_{7/2} and 4f_{5/2} respectively, consistent with successful Ta incorporation. These binding energies fall between those of Ta⁵⁺ (25.90/27.90 eV) and Ta⁴⁺ (23.30/25.20 eV)^{45, 46}, suggesting an intermediate Ta oxidation state (+4 to +5). The slight decrease in average valence is likely caused by oxygen vacancies and other structural defects formed during moltensalt synthesis^{40, 47}. Such valence state is beneficial for the electron donation from Ta to Ru via Ta-O-Ru linkage²⁸. The overlapping region with the O 2s signal was not analysed due to the peak interference. Compared to the commercial RuO₂ (Ru⁴⁺, Ru 3d_{5/2} located at 280.50 eV and $3d_{3/2}$ at 284.70 eV) $^{41, 47, 48}$, the Ru $3d_{5/2}$ peak of the home-made RuO_x shifts by ~0.10 eV toward lower binding energy, indicating a slight electron enrichment around Ru. This modest negative shift is possibly related to the molten salt synthesis as well. Crucially, upon Ta doping (RuO_x-10Ta), the shift further increases to ~0.20 eV, demonstrating a further electron donation to Ru from Ta via the Ta-O-Ru linkage. O 1s XPS deconvolution (Fig. S11d-e) uncovered four oxygen species: lattice oxygen (529.02 eV), oxygen vacancy (530.00 eV), adsorbed -OH (531.30 eV) and adsorbed H₂O (532.86 eV)^{47, 49}. Compared with C-RuO₂, the homemade RuO_x possessed elevated oxygen-vacancy concentration, attributed to the etching effect of the molten salt synthesis^{40, 47, 49}. Significantly, the introduction of Ta increased the amount of lattice oxygen, which was attributable to more surrounding O2- ions for higher valence of Ta and strong binding between Ta and O. The concomitant increase in Ru electron density and lattice oxygen

Journal of Materials Chemistry A

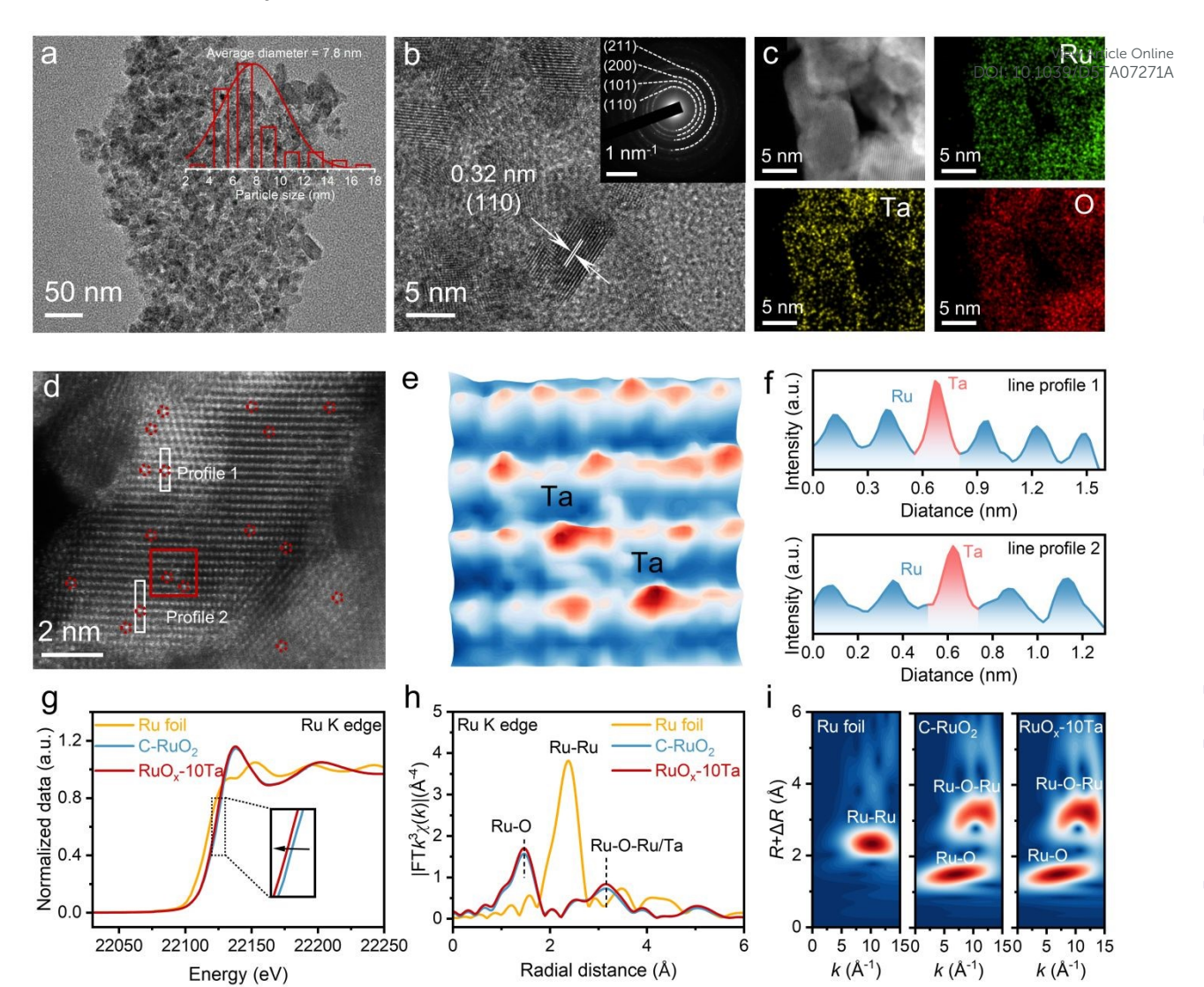


Fig. 1 Structural characterization of RuO_x - α Ta. (a) TEM image with diameter distribution (inset) of the RuO_x -10Ta. (b) HR-TEM image of RuO_x -10Ta with SAED image (inset). (c) Elemental mappings of RuO_x -10Ta. (d) Aberration-corrected HAADF-STEM image. (e) 3D atom-overlapping Gaussian function fitting mapping of the selected red squares area in (d). (f) Intensity profiles along the yellow rectangle regions in (d). (g) Ru K-edge XANES spectra of RuO_x -10Ta and the corresponding reference samples. (h) Fourier transforms of RuO_x -10Ta and the corresponding reference samples. (i) Wavelet transform for RuO_x -10Ta and the Ru-10Ta and the corresponding reference samples.

content suggested the effective electronic modulation by Ta-O-Ru configuration. Besides, no Na-related signal was detected from RuO_x-10Ta (Fig. S11a), further ruling out residual Na and its possible effects on OER performance³⁸. H₂ temperature-programmed reduction (H₂-TPR) (Fig. S12) corroborated tuned bond strength and oxygen lability via Ta doping. RuO_x exhibited a significant shift of the reduction peak to a lower temperature (~50 °C) compared to C-RuO2 indicating enhanced lattice oxygen activity. Upon Ta incorporation, the peak slightly shifted to higher temperature with decreased area and minor splitting, suggesting fewer labile oxygen species for RuO_x-10Ta, which was probably attributable to stronger Ta-O-Ru interactions⁵¹, ⁵². The signal for RuO_x-10Ta remained lower than that of C-RuO₂, indicating that lattice oxygen was maintained in a more activated state relative to C-RuO₂, which implies the appropriate oxygen activity and strong stability of Ta-O-Ru motifs. Furthermore, X-ray absorption spectroscopy (XAS) was employed to probe environment of Ru sites for RuO_x-10Ta. Fig. 1g depicts the Ru K-edge X-ray absorption nearedge structure (XANES) spectrum of RuO_x-10Ta, alongside Ru foil and C-RuO₂ as references. A shift in the absorption edge of RuO_x-10Ta toward lower energy compared to that of C-RuO₂ reference (Fig. 1g) demonstrated a moderately reduced Ru oxidation state (<+4) in RuO_x-10Ta^{25, 53}. This result is in line with XPS data, further verifying the electron transfer in Ta-O-Ru linkages, which increases electron density around Ru sites and thereby prevents overoxidation of Ru during the OER processes. Fourier-transformed extended X-ray absorption fine structure (FT-EXAFS) spectrum (phase-uncorrected) of RuO_x-10Ta at Ru K-edge shows a prominent peak at ~1.55 Å affiliated with the first Ru-O coordination shell, which is identical to rutile RuO₂ (Fig. 1h)²⁵. Quantitative FT-EXAFS fitting reveals an average Ru-O coordination number of 5.68 (Fig. S13 and Table S2), which is significantly lower than the ideal value of 6.00 for octahedrally coordinated Ru in C-RuO2, indicating the generation of oxygen vacancies (O_v) around Ru sites upon Ta incorporation. In addition, the Ru-O bond length shows only a slight increase (1.98 Å for C-RuO₂ and 1.99 Å for RuO_x-10Ta), in good agreement with the

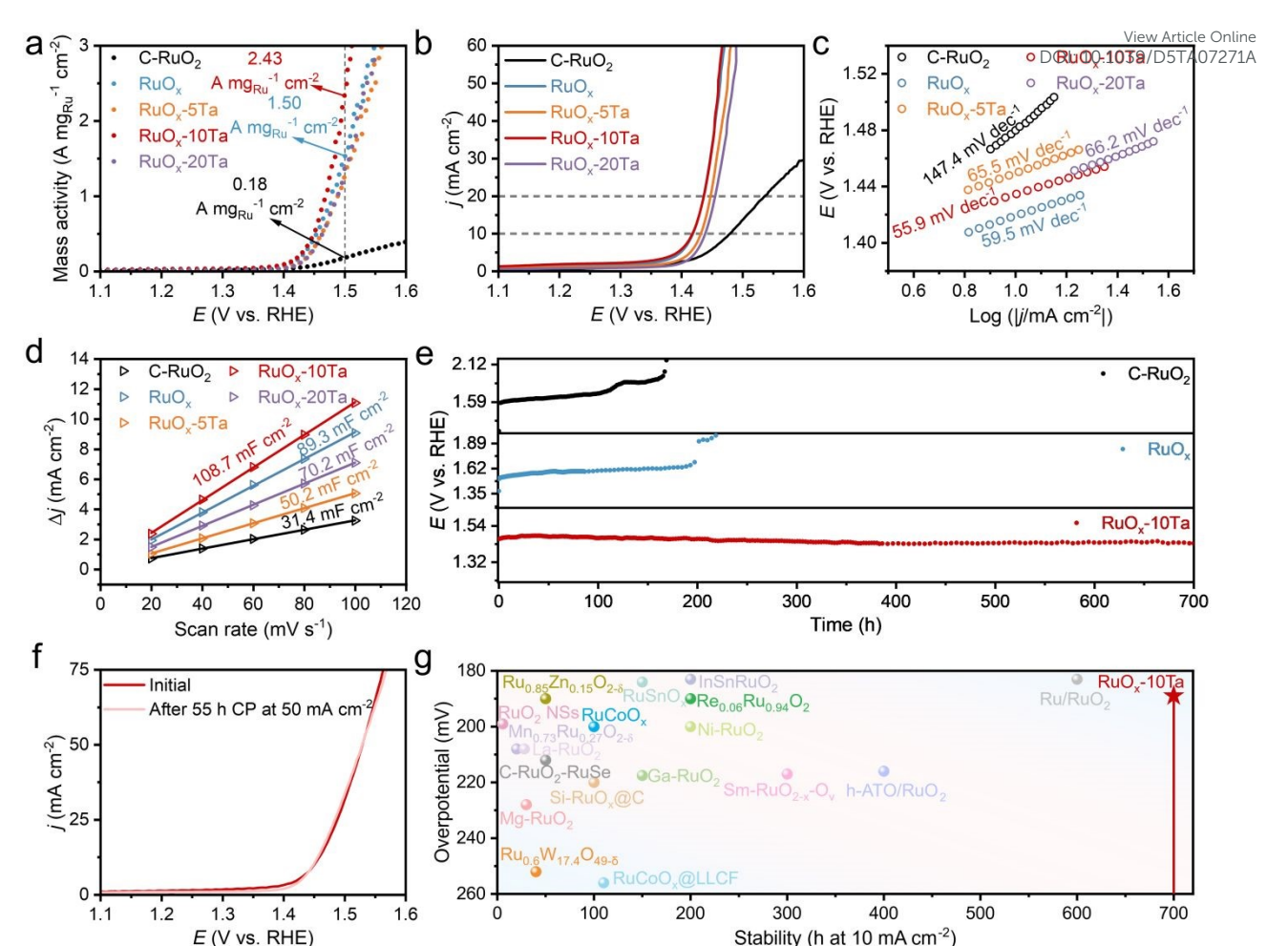


Fig. 2 Electrocatalytic performance. (a) LSV curves normalized by Ru mass of RuO_x- α Ta (α =5, 10 and 20), homemade RuO_x and C-RuO₂. (b) LSV curves of RuO_x- α Ta, homemade RuO_x and C-RuO₂. (c) Tafel plots derived from the polarization curves in (b). (d) Electrochemical double-layer capacitance (C_{dl}) of the electrocatalysts. (e) Chronopotentiometric plots of C-RuO₂, RuO_x and RuO_x-10Ta at 10 mA cm⁻². (f) LSV curves of RuO_x-10Ta before and after 55 h CP at 50 mA cm⁻². (g) Comparison of overpotential and durability at j = 10 mA cm⁻² with previously reported OER catalysts in acidic media.

XRD results. It is thus clear that the overall rutile RuO_2 lattice remains intact despite the introduction of O_v for RuO_x -10Ta. Wavelettransform (WT) analysis, providing simultaneous resolution in k and R-space, allows for the discernment of atoms sharing similar coordination environments and proximities. In Fig. 1i, the WT contour plot of RuO_x -10Ta exhibits enhanced scattering intensity around k = 12 Å-1 compared to C-RuO2, which can be attributed to the heavier element Ta incorporated into RuO_x matrix, further indicating the formation of Ta-O-Ru linkage⁵⁴. Overall, these comprehensive structural and electronic investigations confirm that Ta atoms are atomically dispersed in RuO_x lattice and contributed to fine electronic modulation, which is anticipated to play a pivotal role in the electrocatalytic performance.

2.2 Electrocatalytic performance

The acid OER performance of RuO_x - αTa was systematically evaluated in the three-electrode system. Crucially, RuO_x -10Ta exhibited high mass activity (2.43 A mg_{Ru}^{-1} cm⁻² at 1.5 V vs. RHE), representing a 62% improvement over pure RuO_x (1.50 A mg_{Ru}^{-1} cm⁻²) and 13-fold higher than C-RuO₂ (0.18 A mg_{Ru}^{-1} cm⁻²) (Fig. 2a and Fig. S14), consistent with the TOF (turnover frequency) results (Fig.

S15). It is worth noting that suitable Ta doping is crucial in improving the OER catalytic activity of Ru sites. Less or over Ta doping would bring catalytic activity compromise, which is due to the smaller amounts of Ta-O-Ru active motifs or the excessive site dilution and even phase separation^{28, 55}. In addition, commercial Ta₂O₅ and homemade TaO_x (Fig. S16) exhibited negligible current densities (< 0.2 mA cm⁻²) even at a high potential of 1.70 V vs. RHE, underscoring the intrinsically inert nature of Ta oxides toward OER. In the linear sweep voltammetry (LSV) tests (Fig. 2b), RuOx-10Ta required a low overpotential of only 189 mV to achieve a current density of 10 mA cm⁻², surpassing RuO_x-5Ta (202 mV), RuO_x-20Ta (210 mV) and C-RuO₂ (250 mV) (Fig. S17). Note that RuO_x-10Ta with lower Ru loading still exhibited high performance comparable to RuO_x, further indicating the crucial role of Ta doping in enhancing the intrinsic activity of Ru. The high activity is further reflected by the smallest Tafel slope (55.9 mV dec⁻¹, Fig. 2c), compared to RuO_x (59.5 mV dec⁻¹ 1), RuO_x-5Ta (65.5 mV dec⁻¹), RuO_x-20Ta (66.2 mV dec⁻¹) and C-RuO₂ (147.4 mV dec⁻¹), indicative of favourable OER kinetics^{52, 53}. The double-layer capacitances $(C_{\rm dl})$ were extracted from the cyclic voltammogram (CV) curves in the non-Faradaic region (Fig. 2d and

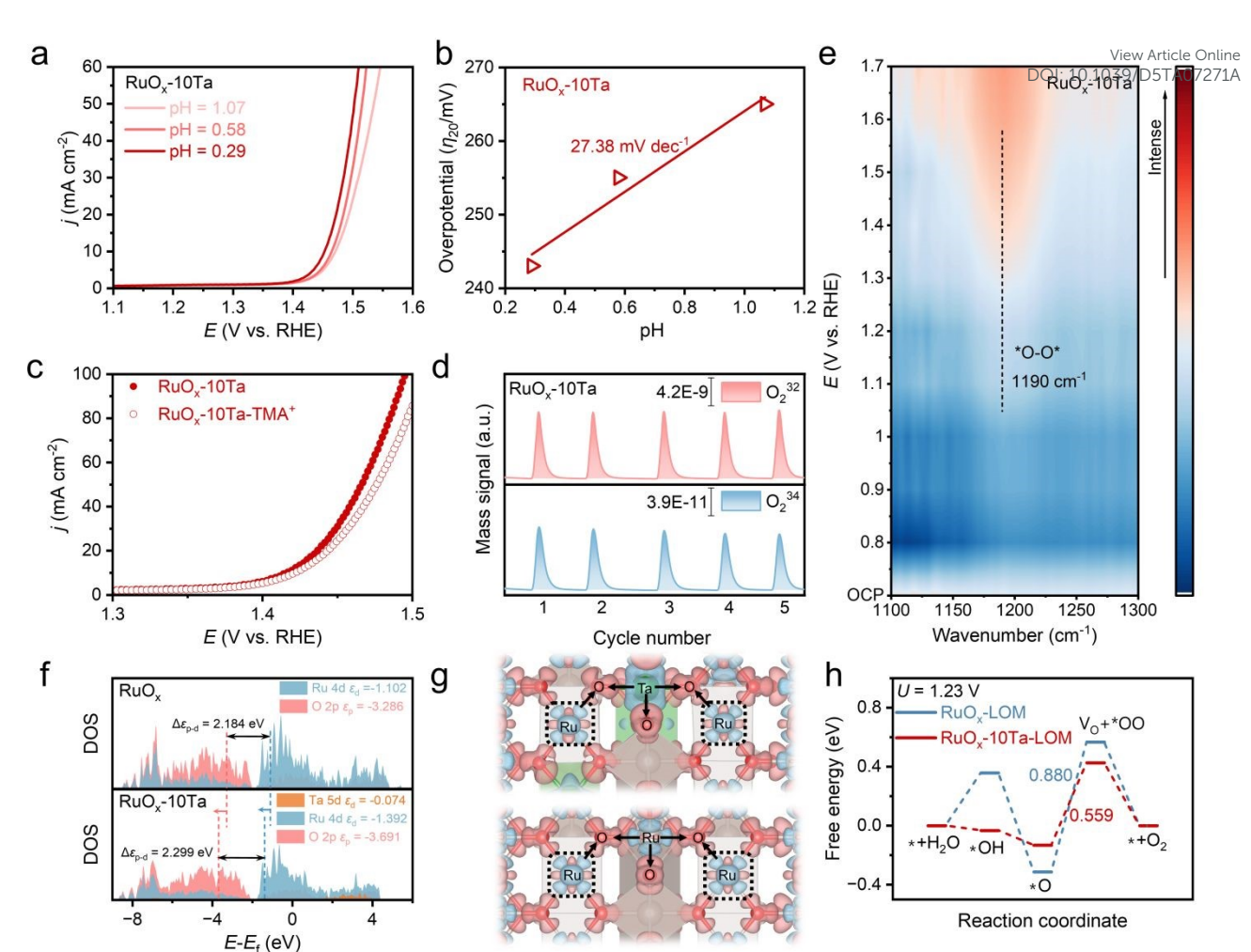


Fig. 3 OER mechanism studies. (a) The pH-dependent LSV curves of RuO_x-10Ta. (b) Overpotentials at 20 mA cm⁻² of RuO_x-10Ta as a function of pH values. (c) LSV curves of RuO_x-10Ta in 0.5 M H₂SO₄ electrolyte with or without TMA⁺. (d) In-situ DEMS with ¹⁸O-labelled measurements for Ta-RuO_x. (e) In-situ ATR-SEIRAS measurements of RuO_x-10Ta. (f) DFT calculated DOS curves for RuO_x and RuO_x-10Ta. (g) DFT calculated CDD maps for RuO_x and RuO_x-10Ta. (h) Free energy diagram of LOM reaction pathways for RuO_x and RuO_x-10Ta at U = 1.23 V.

Fig. S18) for the estimation of the electrochemical surface area (ECSA). RuO_x-10Ta shows the largest $C_{\rm dl}$ (108.7 mF cm⁻²) compared with RuO_x-5Ta (50.2 mF cm⁻²), RuO_x-20Ta (70.2 mF cm⁻²), RuO_x (89.3 mF cm⁻²) and C-RuO₂ (31.4 mF cm⁻²). This highest $C_{\rm dl}$ value for RuO_x-10Ta indicates its largest ECSA, suggesting the most abundant accessible active sites among the series of catalysts. Electrochemical impedance spectroscopy (EIS) further demonstrated the lowest charge-transfer resistance ($R_{\rm ct}$) for RuO_x-10Ta, highlighting the improved charge transfer efficiency introduced by Ta doping (Fig. S19)²⁰.

Moreover, RuO_x-10Ta delivered a long-term durability under acidic OER conditions. At the current density of 10 mA cm⁻² in 0.5 M $\rm H_2SO_4$, RuO_x-10Ta maintains stable performance over 700 hours without apparent decay, far exceeding the pristine RuO_x (less than 200 h) and C-RuO₂ (120 h), and most of the reported Ru-based electrocatalysts (Fig. 2g and Table S4). Even at a higher current density of 50 mA cm⁻² (Fig. S20), RuO_x-10Ta also demonstrated splendid durability for more than 300 h.

Post-OER characterizations corroborated the structural integrity of the catalyst after long-term electrolysis. The RuO_x-10Ta exhibits

negligible variation of LSV curve after 55 hours running at 50 mA cm⁻² (Fig. 2f), demonstrating well activity retention. Additionally, the recovered RuO_x-10Ta remains structurally and compositionally stable. SEM shows a continuous network of connected nanoparticles, and compositional mapping indicates uniform Ru and Ta distributions (Fig. S21). TEM further shows well-dispersed particles with only slight growth (average size: 9.3 nm) and minimal agglomeration (Fig. S22a). The well-resolved lattice fringes and SAED pattern confirmed the retention of the rutile phase (inset of Fig. S22b). Consistently, EDS maps (Fig. S22c-d) show homogeneous Ru and Ta without evidence of phase segregation. High-resolution XPS spectra after OER (Fig. S23) exhibit high-valent Ru⁶⁺ species in RuO_x and C-RuO₂. However, such Ru species were not observed for RuOx-10Ta, suggesting the suppressed Ru overoxidation as a result of Ta doping. This is consistent with the high S-number (stability number, 2.70×10^5) of RuO_x-10Ta, calculated from ICP-MS analysis of the electrolyte after 400 h CP at 10 mA cm⁻². Furthermore, the O 1s spectra revealed a higher lattice oxygen content, as evidenced by a larger peak area in RuO_x-10Ta relative to both undoped RuO_x and C-RuO₂,

Dpen Access Article. Published on 22 10 2025. Downloaded on 2025/11/03 15:12:59.

This article is licensed under a Creative Commons Attribution-NonCommercial 3.0 Unported Licence.

demonstrating better preservation of the oxygen framework under harsh electrochemical conditions.

Additionally, the generality of the asymmetric active unit was further extended by introducing Zr, Hf, and Nb dopants, which also feature strong bonding to oxygen, and adjustable high valence states similar to Ta. All variants exhibited good OER activity with overpotentials below 220 mV at 10 mA cm⁻² (Fig. S24) and significantly prolonged durability at 50 mA cm⁻² than pristine RuO_x (Fig. S25). Structural analyses (XRD, TEM and XPS) confirmed the analogous modulation of crystallinity, Ru oxidation states and oxygen species (Figs. S26-S28), which further affirms that asymmetric M-O-Ru active unit via high-valent doping engineering can effectively enhance the catalyst durability while preserving high activity.

2.3 Mechanism investigation

To unravel the oxygen evolution process on RuO_x-10Ta, electrochemical and in-situ spectral characterizations were performed. First, pH-dependent linear sweep voltammetry (LSV) revealed a clear activity decline with increasing pH on RuO_x and RuO_x-10Ta (Fig. 3ab and Fig. S30), which is a hallmark of lattice oxygen participation process (LOM) as the LOM is inherently sensitive to proton availability^{58, 59}. Furthermore, the tetramethylammonium cations (TMA+) were used as mechanistic indicators. It was found that peroxo-like (*O₂²⁻) intermediates generated via the LOM pathway feature longer lifetimes than superoxo-like (*O₂-) species produced through adsorbate evolution mechanisms (AEM), thus enabling the direct probing of *O₂²- during the OER process^{60, 61}. As the electrophilic site, TMA+ selectively stabilizes the negative *O₂²species through Coulombic trapping, thereby inhibiting the O-O coupling kinetics, and inhibiting the LOM pathway. A marked suppression in OER performance was observed for both RuOx and RuOx-10Ta along with adding 0.1 M TMA+, corroborating the involvement of LOM pathway on RuOx and RuOx-10Ta (Fig. S31 and Fig. 3c). The hypothesis is also strongly supported by in-situ differential electrochemical mass spectrometry (DEMS) using ¹⁸O isotopic labelling⁶², wherein distinct ³⁴O₂ signals were detected (Fig. 3d and Fig. S32) following electrochemical pre-conditioning in H₂¹⁸O (see Experimental Section in Supporting Information). In addition, insitu attenuated total reflection surface-enhanced infrared absorption spectroscopy (ATR-SEIRAS) measurements were carried out to detect the reaction intermediates. As potential increases, the absorption bands at 1170 cm⁻¹ (RuO_x) and 1190 cm⁻¹ (RuO_x-10Ta) exhibit progressive intensification (Fig. S33 and Fig. 3e), which is assignable to the *O-O* intermediate^{20, 63-65}. This observation provides direct molecular spectroscopic evidence that the oxygen evolution reaction on both RuO_x and RuO_x-10Ta catalysts proceeds through the lattice oxygen-mediated pathway. Additionally, in-situ EIS provided further insights into the electrochemical processes on the catalysts (Fig. S34). In the Bode plots, the high-frequency region represents the oxidation of the catalysts, and RuOx-10Ta exhibited a near-zero phase angle, indicating minimal surface oxidation⁶⁶. The low-frequency region corresponds to the interfacial charge transfer during OER. The RuO_x-10Ta exhibited a smaller phase angle, demonstrating facilitated charge transfer and enhanced reaction kinetics of OER^{67, 68}.

To better understand the OER mechanism with the atomically dispersed Ta-O-Ru asymmetric motifs, density functional theory

(DFT) calculations were conducted. Based on the aforementioned analyses, computational models of pristine RuOx and Tardoped RuOx were constructed (Figs. S35-S38). The densities of states (DOS) (Fig. 3f) for RuO_x and RuO_x-10Ta show a downward shift of the O 2p band centre from -3.286 eV (RuOx) to -3.691 eV (RuOx-10Ta) and of the Ru 4d centre from -1.102 eV (RuO_x) to -1.392 eV (RuO_x-10Ta), suggesting a moderately reduced Ru-O covalency and the stabilization of both Ru and O sites^{29, 50, 58}. The gap between the O 2p band and Ru 4d band centres for RuOx-10Ta increases from 2.184 to 2.299 eV (Δ = 0.115 eV), further evidencing a moderate attenuation of the Ru-O covalency, which is favourable for suppressing over-oxidation while stabilizing the lattice oxygen. In addition, the charge density difference (CDD) maps (Fig. 3g) clearly reveal the characteristic charge redistribution induced by Ta doping. Pronounced electron depletion on Ta atoms, along with enhanced electron accumulation on neighbouring O atoms, suggested the strong interaction between Ta and O and the strong Ta-O bond⁶⁹, which is beneficial for stabilizing lattice oxygen. Moreover, this charge redistribution further increases the electron density at adjacent Ru sites with more electron accumulation (Fig. S39) compared to RuOx, consistent with the XAS and XPS results. This would be beneficial for suppressing overoxidation of Ru sites and thereby improving stability⁷⁰. Furthermore, OER pathways were investigated for analysis of their intrinsic activity. Accordingly, the rate-determining step (RDS) of AEM and LOM pathways can be assigned to the formation of *OOH and the generation of V_O + *O₂, respectively. As shown in Fig. 3h and Figs. S35-S36, both RuOx and RuOx-10Ta deliver lower energy barriers (0.880 eV and 0.559 eV) for the RDS of LOM pathways than the AEM (RuO_x: 1.122 eV, RuO_x-10Ta: 0.756 eV). These results indicate that the subtly attenuated Ru-O covalency of RuOx-10Ta preserves the high intrinsic activity through lattice oxygen participation. Note that the kinetic barrier for the initial water dissociation step is significantly reduced on RuO_x-10Ta (Fig. 3h and Figs. S40-S41), in line with the in-situ Raman observations of enriched free-H₂O populations at the Ta-doped interface (Fig. S42)⁶¹, ^{63, 71, 72}. The facilitated water dissociation contributes to the refilling of oxygen vacancies (Vo) by *OH species, limiting excessive lattice oxygen loss and structural degradation^{29, 73}. Overall, the Ta-O-Ru asymmetric motif effectively balances Ru-O bond covalency and strength to favour LOM activity while inhibiting structural degradation.

2.4 Performance of PEMWE devices

Motivated by the high OER performance of RuO_x -10Ta, we constructed a PEM electrolyser using RuO_x -10Ta and 40 wt% Pt/C as anode and cathode catalysts to evaluate the potential of our catalysts in practical application (Fig. 4a). The performance evaluation of all devices was conducted at 60 °C using deionized water. As depicted in Fig. 4b, the PEMWE cell employing RuO_x -10Ta as an anode catalyst achieves a current density of 1 A cm⁻² at a cell voltage of only 1.639 V (1.500 V after *iR* compensation), which is markedly lower than that required by the commercial RuO_2 -based PEMWE system (Fig. S43). Impressively, RuO_x -10Ta exhibits excellent long-term durability, maintaining stable operation for over 200 hours at a high current density of 200 mA cm⁻² (Fig. 4c). The corresponding degradation rate is as low as 3.75 μ V h⁻¹, indicating a negligible performance decay.

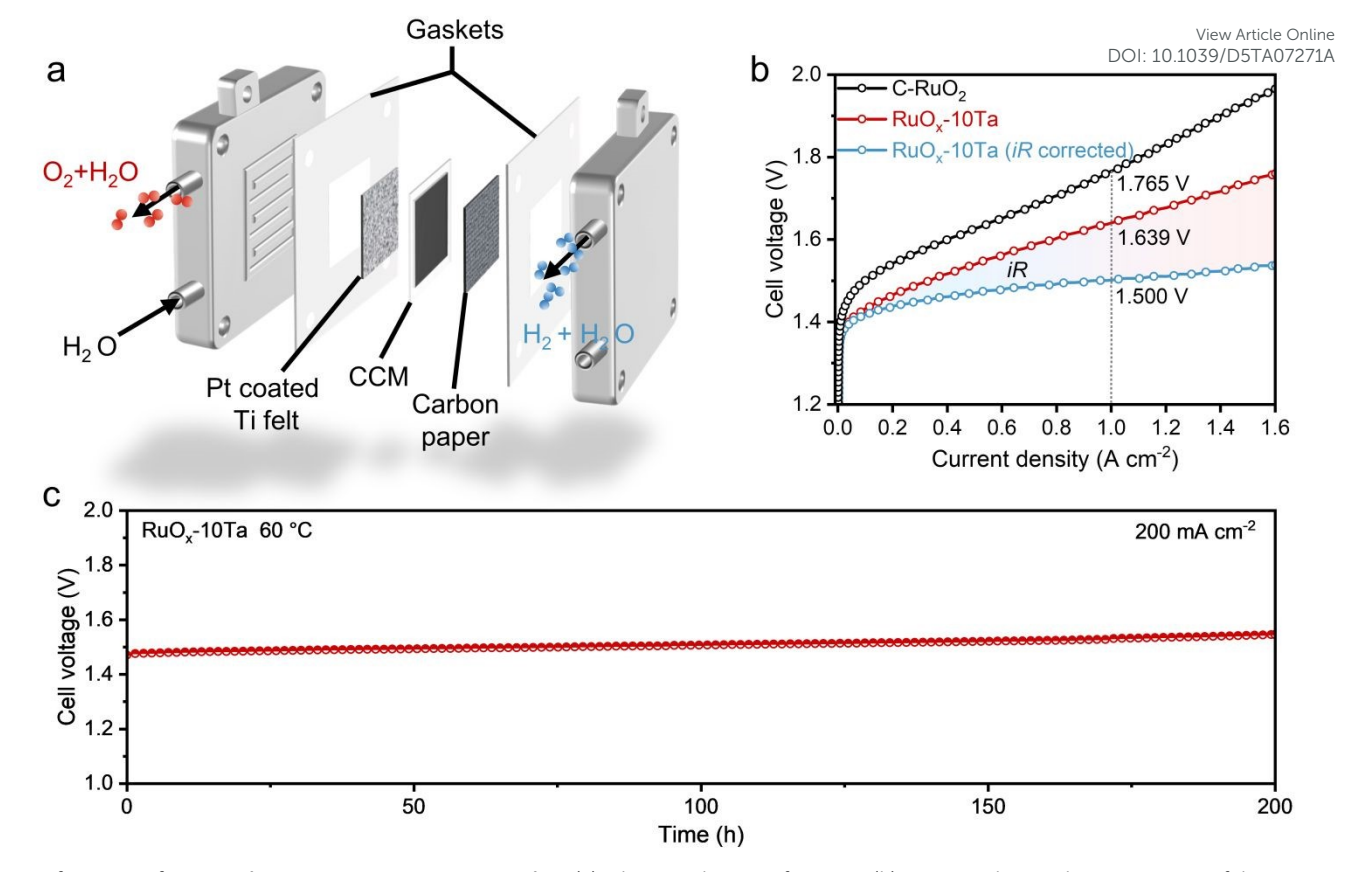


Fig. 4 Performance of PEMWE device using RuO_x-10Ta OER catalyst. (a) Schematic diagram of PEMWE. (b) Current-voltage polarization curves of the PEMWE cell with RuO_x-10Ta and C-RuO₂. (c) The chronopotentiometry curve using RuO_x-10Ta at 60 °C at 200 mA cm⁻².

Overall, these merits indicate the active and stable feature of RuO_{x} -10Ta, with promising practical application prospects.

3 Conclusion

In this work, we overcome the intrinsic activity-stability trade-off in Ru-based acidic OER catalysts by engineering the asymmetric Ta-O-Ru active motifs using atomically Ta doping. Fine-tuning of Ru-O covalency to balance lattice oxygen activity, and strong Ta-O-Ru bond for structural robustness were simultaneously achieved. Combined experimental and theoretical analyses identified the dominant LOM pathway which preserves high activity while ensuring enhanced stability. The resulting RuO_x-10Ta delivers a high mass activity of 2.43 A mg_{Ru}-1 and an exceptional structural robustness under accelerated degradation conditions (700 h@10 mA cm⁻²), realizing about 6-fold lifespan extension over commercial RuO₂. This robustness provides a foundation for high-current-density operation, as demonstrated by the stable operation of a PEMWE device at 200 mA cm⁻² for over 200 hours. This study demonstrates that asymmetric coordination engineering represents a powerful and broadly applicable strategy for enhancing the activity and stability in acidic OER catalysis. It opens avenues for the design of high-performance electrocatalysts based on controlled asymmetric local electronic structures.

Author contributions

Conceptualization: X. Zhang and H. Zhong; methodology: D. Wang, C. Ma, and H. Zhong; validation: T. Liu, C. Ma, and H. Zhong; investigation: C. Ma, N. Zhang, J. Ren and T. Jiang; data analysis and assembly, C. Ma, D. Wang, J. Ren, T. Jiang and Alexandra A. Zverko; writing-original draft preparation: C. Ma and N. Zhang; writing-review and editing: C. Ma, N. Zhang, and H. Zhong; funding acquisition: X. Zhang and H. Zhong. All authors have given approval for the final version of the manuscript.

Conflicts of interest

The authors declare no conflicts of interest.

Data availability

All data supporting the findings of this study are included in the manuscript and its SI. Additionally, the raw datasets are available from the corresponding authors, upon reasonable request.

This article is licensed under a Creative Commons Attribution-NonCommercial 3.0 Unported Licence Downloaded on 2025/11/03 15:12:59. Access Article. Published on 22 10 2025.

Acknowledgements

ARTICLE

This work was supported by the National Key R&D Program of China (2021YFB4000603), the National Natural Science Foundation of China (52273277 and U24A2062), Jilin Province Science and Technology Development Plan Funding Project (SKL202302039) and Youth Innovation Promotion Association CAS (2021223). These authors thank the staff of beamline BL13SSW at the Shanghai Synchrotron Radiation Facility for experiment support. H. Zhong acknowledges funding from the National Natural Science Foundation of China Outstanding Youth Science Foundation of China (Overseas).

Notes and references

- Y. Wang, M. Zhang, Z. Kang, L. Shi, Y. Shen, B. Tian, Y. Zou, H. Chen and X. Zou, Nat. Commun., 2023, 14, 5119.
- H. Gao, Z. Xiao, S. Du, T. Liu, Y. C. Huang, J. Shi, Y. Zhu, G. Huang, B. Zhou, Y. He, C. L. Dong, Y. Li, R. Chen and S. Wang, Angew. Chem., Int. Ed., 2023, 62, e202313954.
- 3. Y. Wang, R. Ma, Z. Shi, H. Wu, S. Hou, Y. Wang, C. Liu, J. Ge and W. Xing, Chem, 2023, 9, 2931-2942.
- Y. Zhou, H. Zhong, S. Chen, G. Wen, L. Shen, Y. Wang, R. Chen, L. Tao and S. Wang, Carbon Energy, 2024, 7, 23146-23157.
- L. Han and Z. Xiang, Fundam. Res., 2025, 5, 624-639.
- C. Rong, K. Dastafkan, Y. Wang and C. Zhao, Adv. Mater., 2023, 35, 2211884.
- C. Xia, F.-M. Li, C. He, S. Zaman, W. Guo and B. Y. Xia, Fundam. Res., 2024, DOI: 10.1016/j.fmre.2024.04.017
- Y. Jia, Y. Li, Q. Zhang, S. Yasin, X. Zheng, K. Ma, Z. Hua, J. 8. Shi, C. Gu, Y. Dou and S. Dou, Carbon Energy, 2024, 6, e528.
- J. Zhao, Y. Guo, Z. Zhang, X. Zhang, Q. Ji, H. Zhang, Z. Song, D. Liu, J. Zeng, C. Chuang, E. Zhang, Y. Wang, G. Hu, M. A. Mushtaq, W. Raza, X. Cai and F. Ciucci, Nat. Nanotechnol., 2025, 20, 57-66.
- 10. M. Bernt, A. Siebel and H. A. Gasteiger, J. Electrochem. Soc., 2018, 165, F305-F314.
- B. Huang, Y. Ma, Z. Xiong, Z. Xiao, P. Wu, P. Jiang and M. Liang, Energy Environ. Mater., 2020, 4, 681-686.
- C. Wei, Z. Wang, K. Otani, D. Hochfilzer, K. Zhang, R. Nielsen, I. Chorkendorff and J. Kibsgaard, ACS Catal., 2023, 13, 14058-14069.
- R. Jiang, D. T. Tran, J. Li and D. Chu, Energy Environ. Mater., 2019, 2, 201-208.
- Y. Wang, H. Yan and H. Fu, eScience, 2024, 5, 100323.
- M. Qi, X. Du, X. Shi, S. Wang, B. Lu, J. Chen, S. Mao, H. Zhang and Y. Wang, J. Am. Chem. Soc., 2025, 147, 18295-18306.
- X. Cao, L. Miao, W. Jia, H. Qin, G. Lin, R. Ma, T. Jin and L. Jiao, Nat. Commun., 2025, 16, 6217.
- Y. Xu, Z. Mao, J. Zhang, J. Ji, Y. Zou, M. Dong, B. Fu, M. Hu, K. Zhang, Z. Chen, S. Chen, H. Yin, P. Liu and H. Zhao, Angew. Chem., Int. Ed., 2024, 63, e202316029.
- L. Zhou, Y. Shao, F. Yin, J. Li, F. Kang and R. Lv, Nat. Commun., 2023, 14, 7644.
- W. He, X. Tan, Y. Guo, Y. Xiao, H. Cui and C. Wang, Angew. Chem., Int. Ed., 2024, 63, e202405798.
- L. Deng, S. F. Hung, Z. Y. Lin, Y. Zhang, C. Zhang, Y. Hao, S. Liu, C. H. Kuo, H. Y. Chen, J. Peng, J. Wang and S. Peng, Adv. Mater., 2023, 35, e2305939.
- J. Chen, Y. Ma, T. Huang, T. Jiang, S. Park, J. Xu, X. Wang, Q. Peng, S. Liu, G. Wang and W. Chen, Adv. Mater., 2024, 36, 2312369.
- J. Chen, Y. Ma, C. Cheng, T. Huang, R. Luo, J. Xu, X. Wang, T. Jiang, H. Liu, S. Liu, T. Huang, L. Zhang and W. Chen, J.

- Am. Chem. Soc., 2025, 147, 8720-8731.
- J. Chen, J. Ma, T. Huang, Q. Liu, X. Liu, B. Luo, 33 X15 X10 Wang, 23. T. Jiang, H. Liu, Z. Lv, T. Yao, G. Wang, X. Zheng, Z. Li, and W. Chen, Angew. Chem., Int. Ed., 2025, 64, e202503330.
- Y. Yu, F. Liu, X. Liu, L. Li, B. Zhou, H. Liao, P. Tan and J. Pan, Chem. Eng. J., 2025, 514, 163295.
- Y. Shen, X. L. Zhang, M. R. Qu, J. Ma, S. Zhu, Y. L. Min, M. R. Gao and S. H. Yu, Nat. Commun., 2024, 15, 7861.
- X. Wang, W. Pi, Z. Li, S. Hu, H. Bao, W. Xu and N. Yao, Nat. Commun., 2025, 16, 4845.
- C. Zhou, L. Li, Z. Dong, F. Lv, H. Guo, K. Wang, M. Li, Z. Qian, N. Ye, Z. Lin, M. Luo and S. Guo, Nat. Commun., 2024,
- H. Liu, Z. Zhang, J. Fang, M. Li, M. G. Sendeku, X. Wang, H. Wu, Y. Li, J. Ge, Z. Zhuang, D. Zhou, Y. Kuang and X. Sun, Joule, 2023, 7, 558-573.
- 29 L. Li, G. Zhang, C. Zhou, F. Lv, Y. Tan, Y. Han, H. Luo, D. Wang, Y. Liu, C. Shang, L. Zeng, Q. Huang, R. Zeng, N. Ye, M. Luo and S. Guo, Nat. Commun., 2024, 15, 4974.
- W. Zheng, Y. Zhao, K. Jiang, F. Xie, L. Meng, S. Gao, J. Li, J. Lan, M. Luo, L. Liu and Y. Tan, Nat. Commun., 2025, 16, 6716.
- Z. Zhang, S. Lu, M. Zhu, F. Wang, K. Yang, B. Dong, Q. Yao and W. Hu, J. Am. Chem. Soc., 2025, 147, 22806-22817.
- B. Yuan, Q. Dang, H. Liu, M. G. Sendeku, J. Peng, Y. Fan, L. Cai, A. Cao, S. Chen, H. Li, Y. Kuang, F. Wang and X. Sun, Nat. Commun., 2025, 16, 4583.
- D. Zhang, M. Li, X. Yong, H. Song, G. I. N. Waterhouse, Y. Yi, B. Xue, D. Zhang, B. Liu and S. Lu, Nat. Commun., 2023, 14,
- X. Ping, Y. Liu, L. Zheng, Y. Song, L. Guo, S. Chen and Z. Wei, Nat. Commun., 2024, 15, 2501.
- W. Hu, B. Huang, M. Sun, J. Du, Y. Hai, W. Yin, X. Wang, W. Gao, C. Zhao, Y. Yue, Z. Li and C. Li, Adv. Mater., 2024, 37, 2411709
- M. Imran, Z. Dai, F. Hussain, W. Xia, R. Chen, F. Wu and L. Li, Energy Storage Mater., 2025, 74, 103950.
- Y. Wang, Y. Zhu, L. Zhang, H. Huang, C. Liu, B. Gao, W. Liu, H. Yan, J. Jian, Z. Huang, J. Feng, T. Yu, Z. Zou and Z. Li, Angew. Chem., Int. Ed., 2025, 64, e202506326.
- N. Zhang, J. Du, N. Zhou, D. Wang, D. Bao, H. Zhong and X. Zhang, Chin. J. Catal., 2023, 53, 134-142.
- Z. Yu, F. Ning, B. Li, Z. Sun, W. Chu and D. Xia, J. Phys. Chem. *C*, 2019, **123**, 18870-18876.
- J. Xu, H. Jin, T. Lu, J. Li, Y. Liu, K. Davey, Y. Zheng, and S.-Z. Qiao, Sci. Adv., 2023, 9, eadh1718.
- C. Hu, K. Yue, J. Han, X. Liu, L. Liu, Q. Liu, Q. Kong, C. Pao, Z. Hu, K. Suenaga, D. Su, Q. Zhang, X. Wang, Y. Tan and X. Huang, Sci. Adv., 2023, 9, eadf9144.
- X. Li, L. Zhou, H. Wang, D. Meng, G. Qian, Y. Wang, Y. He, Y. Wu, Z. Hong, Z.-F. Ma and L. Li, J. Mater. Chem. A, 2021, 9, 19675-19680.
- Y. Wang, R. Yang, Y. Ding, B. Zhang, H. Li, B. Bai, M. Li, Y. Cui, J. Xiao and Z. Wu, Nat. Commun., 2023, 14, 1412.
- J. Yang, K. An, Z. Yu, L. Oiao, Y. Cao, Y. Zhuang, C. Liu, L. Li, L. Peng and H. Pan, ACS Catal. 2024, 14, 17739-17747.
- S. Hao, H. Sheng, M. Liu, J. Huang, G. Zheng, F. Zhang, X. Liu, Z. Su, J. Hu, Y. Qian, L. Zhou, Y. He, B. Song, L. Lei, X. Zhang and S. Jin, Nat. Nanotechnol., 2021, 16, 1371-1377.
- Q. Yu, Z. Zhang, S. Qiu, Y. Luo, Z. Liu, F. Yang, H. Liu, S. Ge, X. Zou, B. Ding, W. Ren, H. M. Cheng, C. Sun and B. Liu, Nat. Commun., 2021, 12, 6051.
- X. Li, G. Chen, Y. Liu, R. Lu, C. Ma, Z. Wang, Y. Han and D. Wang, Energy Environ. Sci., 2025, 18, 4200-4209.
- X. Chen, Y. Cheng, B. Zhang, J. Zhou and S. He, Nat. Commun., 2024, **15**, 6278.
- D. Chen, R. Yu, K. Yu, R. Lu, H. Zhao, J. Jiao, Y. Yao, J. Zhu,

This article is licensed under a Creative Commons Attribution-NonCommercial 3.0 Unported Licence

Open Access Article. Published on 22 10 2025. Downloaded on 2025/11/03 15:12:59.

ARTICLE

View Article Online

DOI: 10.1039/D5TA07271A

- J. Wu and S. Mu, Nat. Commun., 2024, 15, 3928.
- Y. Lin, Z. Tian, L. Zhang, J. Ma, Z. Jiang, B. J. Deibert, R. Ge and L. Chen, *Nat. Commun.*, 2019, 10, 162.
- N. Richards, L. A. Parker, J. H. Carter, S. Pattisson, D. J. Morgan, N. F. Dummer, S. E. Golunski and G. J. Hutchings, *Catal. Lett.*, 2021, 152, 213-226.
- J. Lee, P. Tieu, J. Finzel, W. Zang, X. Yan, G. Graham, X. Pan and P. Christopher, AD, 2023, 3, 2299-2313.
- S. Zuo, Z.-P. Wu, D. Xu, R. Ahmad, L. Zheng, J. Zhang, L. Zhao, W. Huang, H. Al Qahtani, Y. Han, L. Cavallo and H. Zhang, Nat. Commun., 2024, 15, 9514.
- Y. Zhang, N. Cao, K. Wang, M. Yan, X. Zhang and P. Xie, ACS Catal., 2025, 15, 8833-8845.
- F. Ospina-Acevedo, L. A. Albiter, K. O. Bailey, J. F. Godínez-Salomón, C. P. Rhodes and P. B. Balbuena, ACS Appl. Mater. Interfaces, 2024, 16, 16373-16398.
- J. Zhang, L. Xu, X. Yang, S. Guo, Y. Zhang, Y. Zhao, G. Wu and G. Li, *Angew. Chem., Int. Ed.*, 2024, 63, e202405641.
- W. Zhu, F. Yao, K. Cheng, M. Zhao, C. J. Yang, C. L. Dong, Q. Hong, Q. Jiang, Z. Wang and H. Liang, *J. Am. Chem. Soc.*, 2023, 145, 17995-18006.
- Z. Shi, Y. Wang, J. Li, X. Wang, Y. Wang, Y. Li, W. Xu, Z. Jiang, C. Liu, W. Xing and J. Ge, *Joule*, 2021, 5, 2164-2176.
- Y. Pan, X. Xu, Y. Zhong, L. Ge, Y. Chen, J. P. M. Veder, D. Guan, R. O'Hayre, M. Li, G. Wang, H. Wang, W. Zhou and Z. Shao, *Nat. Commun.*, 2020, 11, 2002.
- N. Yao, H. Jia, J. Zhu, Z. Shi, H. Cong, J. Ge and W. Luo, *Chem*, 2023, 9, 1882-1896.
- L. Wu, W. Huang, D. Li, H. Jia, B. Zhao, J. Zhu, H. Zhou and W. Luo, *Angew. Chem.*, *Int. Ed.*, 2024, 64, e202413334.
- C. Lin, J. L. Li, X. Li, S. Yang, W. Luo, Y. Zhang, S. H. Kim, D.-H. Kim, S. S. Shinde, Y. F. Li, Z. P. Liu, Z. Jiang and J. H. Lee, *Nat. Catal.*, 2021, 4, 1012-1023.
- L. Deng, S. F. Hung, S. Liu, S. Zhao, Z. Y. Lin, C. Zhang, Y. Zhang, A. Y. Wang, H. Y. Chen, J. Peng, R. Ma, L. Jiao, F. Hu, L. Li and S. Peng, *J. Am. Chem. Soc.*, 2024, 146, 23146-23157.
- L. Deng, H. Chen, S. F. Hung, Y. Zhang, H. Yu, H. Y. Chen, L. Li and S. Peng, J. Am. Chem. Soc., 2024, 146, 35438-35448.
- S. Zhao, S. F. Hung, L. Deng, W. J. Zeng, T. Xiao, S. Li, C. H. Kuo, H. Y. Chen, F. Hu and S. Peng, *Nat. Commun.*, 2024, 15, 2728.
- S. Zi, J. Zhu, Y. Zhai, Y. Hu, N. Zhang, S. Li, L. Liu, L. An, P. Xi and C. H. Yan, *Angew. Chem., Int. Ed.*, 2025, 64, e202413348.
- X. Y. Zhang, H. Yin, C. C. Dang, H. Nie, Z. X. Huang, S. H. Zheng, M. Du, Z. Y. Gu, J. M. Cao and X. L. Wu, *Angew. Chem., Int. Ed.*, 2025, 64, e202425569.
- Y. Hao, S. F. Hung, W. J. Zeng, Y. Wang, C. Zhang, C. H. Kuo,
 L. Wang, S. Zhao, Y. Zhang, H. Y. Chen and S. Peng, *J. Am. Chem. Soc.*, 2023, 145, 23659-23669.
- X. Zhang, Y. Zhang, B. O. Protsenko, M. A. Soldatov, J. Zhang, C. Yang, S. Bo, H. Wang, X. Chen, C. Wang, W. Cheng and Q. Liu, *Nat. Commun.*, 2025, 16, 6921.
- C. Li, C. Yuan, X. Huang, H. Zhao, F. Wu, L. Xin, X. Zhang, S. Ye and Y. Chen, eScience, 2025, 5, 100307.
- R. Ram, L. Xia, H. Benzidi, A. Guha, V. Golovanova, A. Garzón Manjón, D. Llorens Rauret, P. S. Berman, M. Dimitropoulos, B. Mundet, E. Pastor, V. Celorrio, C. A. Mesa, A. M. Das, A. Pinilla-Sánchez, S. Giménez, J. Arbiol, N. López and F. P. García de Arquer, *Science*, 2024, 384, 1373-1380.
- 72. L. Wu, W. Huang, D. Li, B. Zhao, H. Zhou and W. Luo, *Angew. Chem., Int. Ed.*, 2025, **64**, e202420848.
- N. Zhang, X. Liu, H. Zhong, W. Liu, D. Bao, J. Zeng, D. Wang,
 C. Ma and X. B. Zhang, *Angew. Chem., Int. Ed.*, 2025, 64, e202503246.

View Article Online DOI: 10.1039/D5TA07271A

All data supporting the findings of this study are included in the manuscript and its SI. Additionally, the raw datasets are available from the corresponding authors, upon reasonable request.